Study of Raman Scattering and Hall Effect for the Mg_xZnO_{1-x} /n-Si Photodetector

Saleem H. Trier[1] , Abdulazeez O. Mousa[2]

[1]Department of Environment, College of Science, University of Al- Qadisiyah, Diwaniyah, Iraq
[2]Department of Physics, College of Science, University of Babylon, P.O. Box 4, Babylon, Iraq
E-mail address: [1]Salemhamza79@yahoo.com , [2]Azizliquid_2005@yahoo.com

Summary

In this work Mg_xZnO_{1-x} thin films have been prepared using a chemical spraying pyrolysis (CSP) technique , Mixed solutions Mg_xZnO_{1-x} have been growth at different volumetric percentages (0, 30, 50, 70, and 90)% and deposited on silicon substrates at temperatures (400,450, and 500) ^oC . The crystal structure was examined by using X-ray diffraction (XRD) technique. The results showed that all the films prepared were polycrystalline, showing improvement in the crystal structure by change at temperature. Topography of the surface of the prepared films have been studied by using field emission scanning electron microscopy (FESEM), and energy dispersive X-ray spectroscopy (EDX). It showed that films contain elements (Si, N, O, Zn, and Mg) as expected. Raman scattering have been measured for Mg_xZnO_{1-x}/n-Si thin films at different Mg-content. It exhibits two intense bands at (468 and 872) cm^{-1}, corresponding to the E_2^{high} second-order Raman scattering modes, and second-order mode the $A_1(LO)$, is the first-order mode of ZnO. As it increases Mg-content up to (50)%, the $A_1(LO)$ mode the locate in intensity. The Hall effect have been studied, results showed measurements Hall that the pure ZnO film was negative type (n-type), while Mg_xZnO_{1-x} films were (p-type).

Keywords: Photodetector, CSP , Substrate Temperature, Raman Scattering

1- Theoretical Part
1-1 X-Ray Diffraction (XRD)

X-ray diffraction peaks consist of interference construction monochrome rays reflected from any position of lattice levels at certain angles. It can calculate the distance interfaces between the levels of the diffraction angle at a certain peak by using (Bragg's law) [1].

$$n \lambda = 2d_{hkl} \sin\theta_B \qquad (1)$$

Where n integer number that represents interference degree (n=1,2, 3,…), λ is the wavelength of the X-ray (1.54) Å [1] , d_{hkl} is the spacing between diffracting planes and θ_B is the Bragg's angle. Normally XRD is used to calculate different parameters which could be used to clarify the studies of the deposited films such as:

1-2 Lattice Constants

The many crystal phases available in transparent conductive oxides (TCOs), hexagonal structure is the dominant phase in ZnO material, hexagonal phase is characterized by determining the (a and c) are lattice constants from X-ray spectrum and by using the following formula [2,3]:

$$\frac{1}{d_{hkl}^2} = \frac{4}{3}\left(\frac{h^2+hk+k^2}{a^2}\right) + \frac{l^2}{c^2} \qquad (2)$$

Where (hkl) are Miller indices ,the a-parameter is obtained from the plane (h00), while the plane (00l) is used to obtain c-parameter. In the case of cubic diamond phase such as crystallite silicon, the a-lattice constant can be obtained from [4]:

$$\frac{1}{d_{hkl}^2} = \left(\frac{h^2+k^2+l^2}{a^2}\right) \qquad (3)$$

1-3 Full Width at Half Maximum

The β of the preferred orientation (peak) could be measured, since it is equal to the width of the line profile (in radian) at the half of the maximum intensity.

1-4 Average Crystallite Size

The single line method is one of the several line profile analysis methods based on a Voigt function to determine the size–strain parameters (microstrains and crystallite sizes). The reason behind the peak shifting was the change of stress, firstly due to the increase in temperature additionally due to the increase in Mg-concentration. The lower boundary of the crystallite size D_s of the films was estimated using the full width at half maximum (FWHM) of (002). The average crystallite size D_s, which can be estimated using the Debye Scherer's formula [4].

$$D_s = \frac{k\,\lambda}{\beta\,\cos(\theta)} \qquad (4)$$

Where k=0.94 is the shape factor, λ is the wavelength of incident X-ray, β is the FWHM measured in radians and θ is the Braggs angle of diffraction peak. The FWHM of the peak corresponds to (002) plane was narrowed with increasing temperature, indicating improvement in crystallinity [4].

1-5 Microstrains

The microstrains are caused during the growth of thin films, and will be raised from stretching or compression in the lattice to make a deviation in the c-lattice constant of the hexagonal structure of the ASTM values. So the strain broadening is caused by varying displacements of the atoms with respect to their reference lattice position. This strain can be calculated from the formula [5]:

$$S = \frac{\beta\,\cos(\theta)}{4} \qquad (5)$$

1-6 Dislocation Density

Dislocations (δ_D) are an imperfection in a crystal associated with misregistry of the lattice in one part of the crystal with respect to another part. Unlike vacancies and interstitial atoms, dislocations are not equilibrium imperfections, i.e. thermodynamic considerations are insufficient to account for their existence in the observed densities. In fact, the growth mechanism involving dislocation is a matter of importance. In the present study, the dislocation density (δ_D) can be calculated using the following relation [2].

$$\delta_D = \frac{1}{D_s^2} \qquad (6)$$

Where D_s is the crystalline size.

1-7 Number of Layers

The number of crystalline layers (N_ℓ) which could be calculated due to the percolation theory, and it depends on the film thickness (t) as the relation [6]:

$$N_\ell = \frac{t}{D_s} \qquad (7)$$

Where D_s is a mean crystallite size or average crystallite size.

2- Field Emission Scanning Electron Microscopy

FESEM is one of the widely instruments used in material research laboratories. In this technique, electrons are used instead of light waves to see the microstructure of surface of a specimen. However since electrons are excited to high energy (KeV), so wavelength of electron waves are quite small and resolution is quite high. Applications of FESEM include semiconductor device cross section analyses for gate widths, gate oxides, film thicknesses, construction details, small contamination feature geometry, and elemental composition measurement. Compared with convention scanning electron microscopy SEM, field emission scanning electron microscopy(FESEM) produces clearer, less electrostatically distorted images with spatial resolution down to (1.5)nm (3 to 6) times better[7].

3- Hall Effect

When a conductor is placed in a magnetic field and a current passed through it an electric field will be produced, the direction of which is normal to both the current and magnetic field directions. This phenomenon, discovered by E.T. Hall in 1879, is known as the Hall effect [8].

$$R_H = \frac{V_H}{I_x} \cdot \frac{t}{B_Z} \qquad (8)$$

The Van der Pauw method which was first propounded by L.J. Van der Pauw in 1958 is often used to measure the Hall effect, which characterizes a sample of semiconductor material and can be successfully completed with a current source, voltmeter, and a magnet. From the measurements made, the following properties of the material can be calculated [9]. The doping type (i.e. if it is a p-type or n-type) material.

- The sheet carrier density of the majority carrier (the number of majority carriers per unit area). From this, the density of the semiconductor, often known as the doping level, can be found for a sample with a given thickness.

- The mobility of the majority carrier.

In order to use the Van der Pauw method, the sample thickness must be much less than the width and length of the sample. In order to reduce errors in the calculations, it is preferable that the sample is symmetrical. There must also be no isolated holes within the sample for a simple metal where there is only one type of Hall voltage V_H is given by:

$$V_H = \frac{-iB/t}{n_e q} \qquad (9)$$

Where B is magnetic field, the Hall coefficient is defined as:

$$R_H = \frac{E_y}{j_x B} = \frac{V_H}{iB/t} = -\frac{1}{n.q} \qquad (10)$$

The simple formula for the Hall coefficient given above becomes more complex in semiconductors where the carriers are generally both electronic and holes which may be present in different concentrations and have different motilities for moderate magnetic fields the hall coefficient is:

$$R_H = \frac{-n_H \mu_e^2 + p_H \mu_h^2}{q(n_H \mu_e + p_H \mu_h)^2} \qquad (11)$$

For large applied fields the simpler expression analogous to that for a single carrier type holds [10].

$$R_H = \frac{1}{(p_H - n_H)q} \qquad (12)$$

Hall mobility μ_H could be calculated from the product of the conductivity σ, and the Hall coefficient according to the equation.

$$\mu_H = \sigma R_H \qquad (13)$$

4- Raman Spectroscopy

Raman spectroscopy is a technique that investigates a sub-category of a material's vibration conditions using monochromatic light. The activities of this technique are represented in its ability to convey the information about the characteristic vibrations of the material, both optical and electronic. During irradiation, the spectrum of the scattered radiation is measured at (90) deg with an appropriate spectrometer. The intensities of the Raman lines are (1)% of the intensity of the source, which could be Stokes scattering. The emitted radiation produces three types of scattering signal: the first two types are Stokes and anti-Stokes scattering that represent less than (1)% of the scattering radiation, while the third type is Rayleigh scattering as shown in fig. 1, which accounts for more than (99)%.
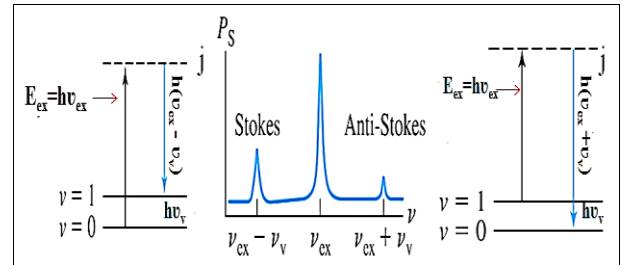

Fig. 1: Schematic of the Stokes and anti-Stokes Transition with a Raman Shift [11]

The first type refers to the indicator for Raman spectroscopy, but not all of it because the anti-Stokes lines are appreciably less intense that the corresponding Stokes lines . As shown in fig.2. Thus, only the Stokes part of the spectrum is generally used. The magnitude of the Raman shifts is independent of the excitation wavelength. The Raman spectrum is represented by the wavenumber shift Δv, which is defined as the difference in wavenumbers (cm^{-1}) between the observed radiation and that of the source. The Stokes and anti-Stokes types are different from the Rayleigh radiation in terms of their frequencies corresponding to $\pm \Delta E$, the energy of

the first vibrational level of the ground state. If the bond was infrared active, the energy of its absorption would also be ΔE. Thus, the Raman frequency shift and the infrared absorption peak frequency is identical [11]. Rayleigh scattering has a considerably higher probability of occurrence than Raman because the most probable event is the energy transfer to molecules in the ground state and reemission by the return of these molecules to the ground state (>99%). The relative population of the two Stokes emissions is much favored over anti-Stokes. The ratio of anti-Stokes to Stokes intensities increases with temperature because a larger fraction of the molecules is in the first vibrationally excited state under these circumstances.
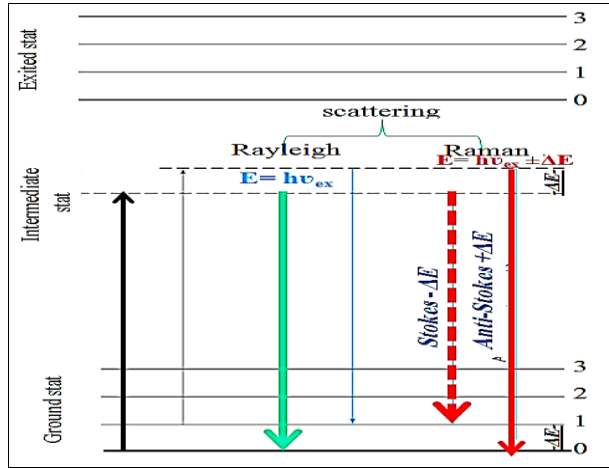

Fig. 2: Schematic Diagram Showing the Types of Transition of the Electrons and the Rayleigh and Raman Scattering [11]

The most important property of Raman spectroscopy is that the energy shifts observed in a Raman experiment should be identical to the energies of its infrared absorption bands, provided that the vibrational activities involved are active with both infrared absorption and Raman scattering [12]. The differences between a Raman spectrum and an infrared spectrum depend on the real conditions between them, that is, the dipole moment. Infrared absorption requires that a vibrational mode of the molecule has a change in dipole moment or the charge distribution associated with it. Scattering involves a momentary distortion of the electrons distributed around a bond in a molecule,

followed by reemission of the radiation as the bond returns to its normal state.

In its distorted form, the molecule is temporarily polarized, which momentarily develops an induced dipole that disappears upon relaxation and reemission. The Raman activity of a given vibrational mode may differ markedly from its infrared activity. The intensity of the Raman peak depends in a complex way on the polarizability of the molecule, the intensity of the source, and the concentration of the active group. The power of the Raman emission increases with the fourth power of the frequency of the source, however, advantage can rarely be taken of this relationship because of the probability that ultraviolet irradiation will cause decomposition by the light. Raman intensities are usually directly proportional to the concentration of the active species. Polarization is a property of a beam of radiation and describes the plane in which the radiation vibrates. Raman spectra is excited by plane-polarized radiation. The scattered radiation is found to be polarized to various degrees depending on the type of vibration responsible for the scattering [13].

4-1 Raman Spectroscopy of ZnO Thin Films

ZnO has the wurzite structure with C_{6V} symmetry. It is a polar uniaxial crystal and it has no centre of inversion-therefore it has piezoelectric properties. The wurzite lattice has (4) atoms per unit cell. The Raman active zone centre phonon vibrations predicted are: one A_1 mode, one E_1 mode and two E_2 modes, (group theory also predicts two B_1 modes but these are silent). The infrared active vibrations are the A_1 and E_1 modes. In wurzite ZnO long range electrostatic forces dominate over the short range interatomic forces. This leads to a split into longitudinal and transverse components of the phonon normal modes that are infrared active i.e. the A_1 and E_1 modes will be split. There will be $A_1(TO)$, A_1 (LO), $E_1(TO)$ and $E_1(LO)$ vibrational modes in the Raman spectrum of ZnO as well as the two E_2 modes (TO=Transverse Optical and LO=Longitudinal Optical). Many experiments have been carried out to distinguish which peak values correspond to which normal modes [14]. To do this, the incident radiation must be polarized, the direction of propagation of the

incident light must be controlled and the scattered radiation must be analyzed.

4-2 Impurities and Defects

The translational symmetry of a crystal is what defines a phonon. If impurities or defects break this translational symmetry, new modes can occur. Localized modes occur when their frequency is too large to propagate through the crystal like a normal phonon . These modes can be known as band modes (non-localized) when the defect or impurity atom is heavier than the lattice atoms surrounding it. In a diatomic crystal, as in the case of ZnO and Mg_xZnO_{1-x} for small(x)%, if a lighter atom replaces the heavier atom, localized modes and gap modes occur. Localized modes are ones whose frequencies occur higher than the perfect lattice frequencies i.e. all acoustic and optical modes. Gap modes have frequencies between bands of allowed modes (i.e. between the acoustic and optical modes in ZnO). Band modes occur within bands of perfect lattice frequencies i.e. between the TA and LA modes or between TO and LO modes[14].

2- Experiment Part
2-1 Silicon Substrate

Si-wafer was n-type (111) with resistivity about (1.5-5)Ω.cm and (500$\pm$10)μm thickness. Square-shaped n-type silicon samples, each of (1.5$\times$1.5) cm^2 area were prepared using a steel-cut machine. Silicon wafers were washed ultrasonically in distilled water and were immersed in ethanol with a purity of (99.9)% in order to remove dirt and oil, while native oxide layer removed by etching in dilute (2:10) HF: H_2O for (3) min. the silicon wafers were cleaned in distilled water and dried in furnace at (373) K.

2-2 Preparation of the Spray Solutions

Films of Mg_xZnO_{1-x} with different Mg-contents were deposited on a glass substrate by chemical spray pyrolysis (CSP) technique under ambient atmosphere. Two kinds of aqueous solutions, Zinc acetate $Zn(CH_3COO)_2.2H_2O$ of (99.9) % purity and molecular weight equal to (219.52)g/mol and Mg acetate $Mg(CH_3COO)_2.4H_2O$ of (99.2) % purity and molecular weight equal to (214.46)g/mol, were chosen as the sources of zinc and magnesium

respectively. In order to obtain Mg_xZnO_{1-x} thin film with different Mg-contents (x= 0,30, 50, 70, and 90)%, the deposition parameters were the same for the series of Mg_xZnO_{1-x} thin film. The pure Zinc acetate , pure Magnesium acetate, and distilled water were mixed thoroughly to get the solution with a concentration of (0.1) M and a few drops of glacial acetic acid were then added to stabilize the solution were added to (100) mL solution to increase the solubility of the compounds. The substrate temperatures were (673,723 and 773) K during the films growth. The solution was stirred for (30)min. with a magnetic stirrer.

3- X-Ray Diffraction (XRD)

The crystal structure and crystallinity of as-grown Mg_xZnO_{1-x} thin film such as nanocrystallite size, structure aspect layer and lattice constant have been investigated by X-ray diffraction (XRD) using SHIMADZU X-ray diffractometer system (XRD-6000) which record the intensity as a function of Bragg's angle. The sample is scanned from (20-60) degree. The conditions of the system were:
- Source CuK_α with radiation of wavelength λ = (1.54) Å.
- Target: Cu
- Current emission = (30) mA.
- Applied voltage = (40) KV.
- Scanning speed = (5) deg./min.

4 - Field Emission Scanning Electron Microscopy

The morphological properties of the Mg_xZnO_{1-x}/n-Si photodetector were investigated by (FESEM) and energy-dispersive X-ray spectroscopy (EDX). The (FESEM) is type (S-4300 of Hitachi, S-4700 FESEM) in Islamic Republic of Iran/ University of Tehran / Razi foundation. The FESEM is used in its common mode, the field mode and the emission mode. In this mode, electrons fired from the electronic gun are accelerated with a voltage (15) KV, which consisting of two magnetic lenses. The main aim of these lenses is to focus a fine electron beam onto the sample. Scanning coils placed before the final lens causes the electron spot to scan across the sample surface in the form of a square raster. The current that passes

through these coils which are typically made to pass through the deflection coils of the cathode ray tube and regenerated on a computer screen to generate the image. There is an interaction between the atoms and electrons in the sample. This interaction causes various signals to generated and the most commonly used signals are those from secondary back-scattered electrons. The secondary electrons are electrons of very low energy and thus, contain information of only a few angstroms deep on the surface of the layer. These electrons are then detected by a detector consisting of a scintillator-photomultiplier combination, which in turn through the system electronics drive the cathode ray tube. These images are the ones commonly used in FESEM to interpret the morphology of a sample.

5- Hall Effect Measurements

Hall effect system (Ecola, Hall effect measurement system, HMS-3000) was used in the present study. Hall measurement is widely used in the initial characterization of semiconductor to determine the following characteristics: electrical resistivity(ρ), electrical conductivity(σ), carrier mobility(μ), Hall coefficient (R_H), carrier concentration (n), and type carrier (n or p).

6 - Raman Shift Measurements

The Raman scattering spectroscopy (RSS) measurements for the thin film Mg_xZnO_{1-x} /n-Si photodetector were investigated by (RSS) in Islamic Republic of Iran / University of Saniti Sharif / Sharif spectroscopy laboratory. Raman spectroscopy is a spectroscopic technique based on inelastic scattering of monochromatic light, usually from a laser source. Inelastic scattering means that the frequency of photons in monochromatic light changes upon interaction with a sample. Photons of the laser light are absorbed by the sample. Frequency of the photons is shifted up or down in comparison with original monochromatic frequency, which is called to increase tontent shifted toward larger angles.

the Raman effect. This shift provides information about vibrational, rotational and other low frequency transitions in molecules. Raman spectroscopy can be used to study solid, liquid and gaseous samples.

3- Results and Discussion
3- 1 (XRD) Analysis of ZnO/n-Si, and Mg_xZnO_{1-x}/n-Si Thin Films

Fig.1 shows the XRD spectrum of ZnO thin films grown on silicon substrate with different Mg-contents (0,30,50,70, and 90)%. At a temperature (450) ^{o}C there are three prominent diffraction peaks viz. (100), (002), and (101) which corresponding to different angle (31.65^{o}, 34,5^{o}, and 36.31^{o}), respectively belong to the hexagonal wurtzite structure of ZnO has been observed see table 1. It can be concluded that the thin films deposited in these experimental conditions show strong c-axis (002) orientation growth. When mixing Mg-content ratios referred to previously, and when certain conditions arise, there are three phases, the first phase remains structure of the hexagonal wurtzite, but down the intensity of the diffraction peaks, the second phase turns into a mixture of MgO is incorporated with ZnO, the third phase turns into the cubic rock salt structure for the appearance of MgO diffraction peaks are clear. In the first case, (i.e. when the Mg-content (50)% we note the appearance of two peaks additional with directions(111),(200) corresponding to the angles of diffraction (36.87^{o}and 42.85^{o}), respectively. While in the third case, (i.e. when the Mg-contents (70 and 90)% we note to increase the intensity of new peaks and the weakness of ZnO peaks and then vanish these results are consistent with research [15]. It remains to refer to the diffraction peaks with increase of Mg-content shifted toward larger angles. All parameters were calculated and included in the table 1. At a temperature of (450) ^{o}C we note that the peaks increasing in strength and its average crystalline size smaller.

Table 1: The G_s, δ_D, S, and N_ℓ of Layers data of (002),(200) Orientations for Mg_xZnO_{1-x}/n-Si at Different Mg-content, and Substrate Temperature (450) ^oC.

Sample	Investigated line(hkl)	2θ (deg.)	d(nm)	FWHM (β) (deg.)	Crystallite Size D(nm)	$\delta_D \times 10^{15}$ (lin m^{-2})	$S \times 10^{-2}$ (lin^{-2} m^{-4})	(N_ℓ)
ZnO	(100)	31.65	2.823	0. 234	70.42	0.2017	5.63	1.14
	(002)	34.50	2.596	0.270	61.40	0.2653	6.47	1.30
	(101)	36.31	2.471	0.200	83.44	0.1436	4.76	0.96
$Mg_{0.3}ZnO_{0.7}$	(100)	31.66	2.823	0.256	62.18	0.2586	6.38	1.29
	(002)	34.65	2.586	0.307	54.24	0.3399	7.32	1.47
	(101)	36.35	2.468	0.223	74.70	0.1792	5.32	1.07
$Mg_{0.5}ZnO_{0.5}$	(100)	31.75	2.815	0.246	64.20	0.2426	5.91	1.19
	(002)	34.72	2.581	0.350	47.56	0.4421	8.35	1.68
	(101)	36.35	2.468	0.209	80.00	0.1563	4.96	1.00
	(111)	36.87	2.435	0.358	46.82	0.4562	8.48	1.71
	(200)	42.85	2.108	0.387	44.12	0.5137	9.00	1.81
$Mg_{0.7}ZnO_{0.3}$	------	-----	-----	------	------	------	-------	------
	(002)	34.75	2.578	0.325	51.28	0.3803	7.75	1.56
	(101)	36.32	2.471	0.197	82.76	0.1460	4.68	0.99
	(111)	36.85	2.436	0.312	53.72	0.3465	7.39	1.49
	(200)	43.05	2.098	0.357	47.80	0.4377	8.30	1.68
$Mg_{0.9}ZnO_{0.1}$	-----	------	------	------	------	------	------	------
	(002)	34.67	2.584	0.395	42.18	0.5621	9.42	1.90
	(101)	36.40	2.465	0.325	51.40	0.3785	7.72	1.56
	(111)	36.87	2.435	0.442	37.92	0.6954	10.47	2.11
	(200)	42.87	2.107	0.339	50.36	0.3943	7.88	1.59

3- 2 Field emission Scanning Electron Microscopy (FESEM) for Mg_xZnO_{1-x}/n-Si Thin Films

The composite Mg_xZnO_{1-x}/n-Si films were measured nanostructure in the Islamic republic of Iran/ university of Tehran/ Razi foundation. Surface morphologies of (FESEM) images and their corresponding (EDX) spectra at different Mg-content (0,30,50,70 and 90)%, and temperature of (450) °C are shown in the Figs.(4 A,B, C , D, and E) respectively. The morphology of the surface of pure ZnO is a nanostructure cannot determine its kind, as irregular in shape, as shown in fig.2 A. From the (FESEM) images the grain size values are found to be in the range of (30-63)nm. When add certain compensatory ratios of Mg-content into ZnO reduced surface roughness gradually as shown in figs.(4 B, C, D, and E). Decrease the grain size in the range of (26-54, 21-43,26- 58,15-24)nm corresponding to the concentrations of Mg-contents (30,50,70, and 90)%, respectively. These values were compared with the results of XRD, as shown in table 2, these results are comparable with other results [15]. Grains with large sizes of (100) nm and above represent drops of material deposited in the film, which is considered as a latent defect in the film and this seems obvious when the ratio (90)% of Mg-content.

Table 2: Comparison between the Grain Size Calculated from (XRD) and (FESEM) Analysis for Mg_xZnO_{1-x}/n-Si Photodetector.

Substrate Temperature(450) ^oC		
Contents	**Crystallite Size Calculated from (XRD) (nm)**	**Grain Size Calculated from (FESEM) Images (nm)**
ZnO (Pure)	47.30	30-63
$Mg_{0.3}ZnO_{0.7}$	52.00	26-54
$Mg_{0.5}ZnO_{0.5}$	31.60	21-43
$Mg_{0.7}ZnO_{0.3}$	37.76	26-58
$Mg_{0.9}ZnO_{0.1}$	38.20	15-24

3-3 Elemental Analysis for Mg$_x$ZnO$_{1-x}$/n-Si Photodetector

The energy-dispersive X-ray analysis spectra (EDX) of the Mg$_x$ZnO$_{1-x}$/n-Si photodetector deposited on silicon substrate at (450)^{o}C by (CSP) technique with different Mg-contents (x = 0, 30, 50, 70, and 90)% are given in figs.(2 a, b, c , d and e). Among the above ratios, the ratio (30)% is the best, when measuring the concentration ratio mentioned at different temperatures was the best temperature is (450) ^{o}C. Which show that all the films contain the elements (Si, N, O, Zn, and Mg) as expected, indicating formation of the Mg$_x$ZnO$_{1-x}$/n-Si photodetector. Fig. 2a shows the (EDX) spectra of the (pure) ZnO film and it reveals that the compound percentage for the (Si, N,O, and Zn) are (73.16, 4.64 ,12.26, and 9.94) respectively. Fig.2b depicts the (EDX) spectra of the Mg$_{0.3}$ZnO$_{0.7}$/n-Si photodetector with compound percentage for the (Si, N, O, Zn, and Mg) are (72.29,6.82,10.55,6.64,and 3.70) respectively these results are similar behavior into [16]. The remaining percentages listed in table 3. The best temperature is (450) ^{o}C. The (EDX) spectrum for all films are clearly observable (SiKα ,ZnLα, MgKα, OKα and NKα lines). Lines did not show ZnKα, ZnKβ in the (EDX) spectra. The adhesion between the MgZnO species and the Si substrate was strong , resulting in higher growth speed in the vertical direction, was the reason why the grain size of MgZnO nanoparticles was lower than those on the Si [17]. Which led to increase the intensity of spectral lines by adding Mg-content.

Table 3: Compound Percentage of the Mg$_x$ZnO$_{1-x}$ /n-Si Photodetector.

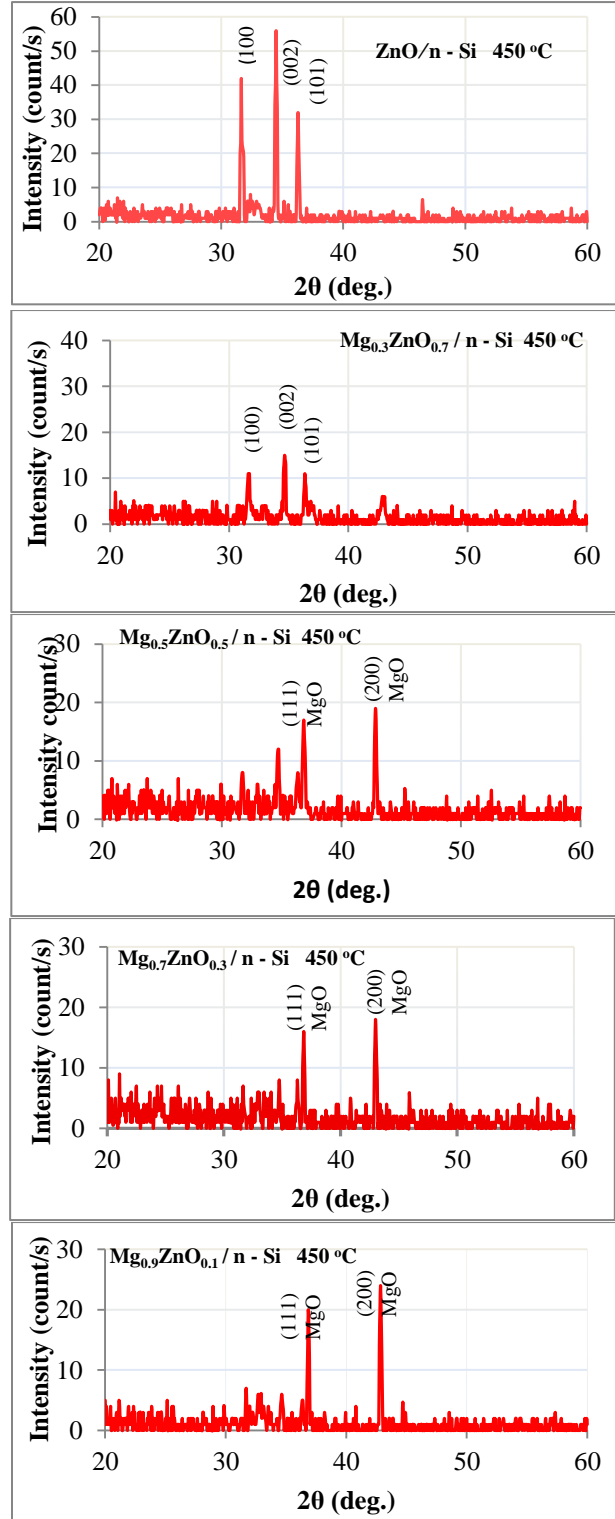| MgO-Contents	Compound Percentage (%)					Total
	Si	N	O	Zn	Mg	
ZnO (Pure)	73.16	4.64	12.26	9.94	0	100
Mg$_{0.3}$ZnO$_{0.7}$	72.29	6.82	10.55	6.64	3.70	100
Mg$_{0.5}$ZnO$_{0.5}$	74.09	3.92	11.60	3.55	6.84	100
Mg$_{0.7}$ZnO$_{0.3}$	73.67	4.57	11.66	1.40	8.70	100
Mg$_{0.9}$ZnO$_{0.1}$	73.18	4.69	12.16	0.52	9.45	100

Fig.1: XRD patterns for Mg$_x$ZnO$_{1-x}$/n -Si Photodetector with Mg-contents (0,30,50,70, and 90)% and at (450) ^{o}C.
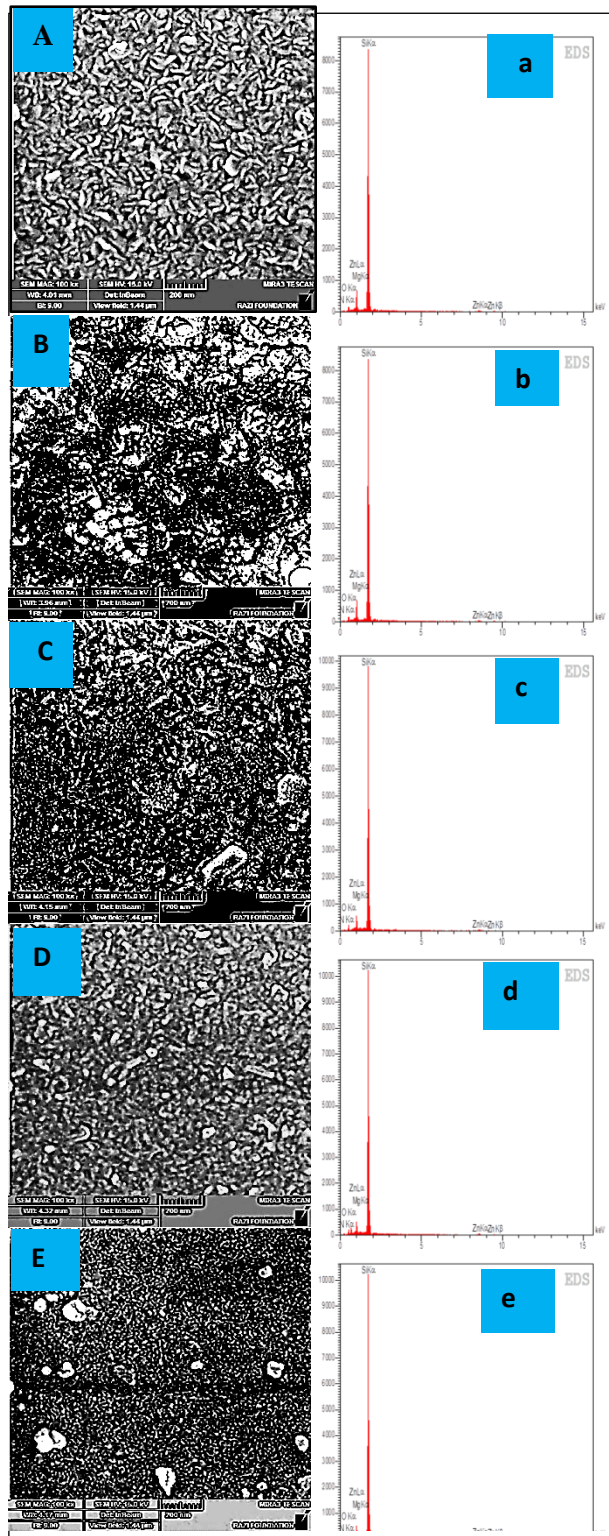
Fig.2: FESEM and EDX for Mg_xZnO_{1-x}/n-Si Photodetector for Mg-Contents (0,30,and 50,70, and 90)% Prepared, at Substrate Temperature(450) ^{o}C.

3-4 Hall Effect Measurements of ZnO, and Mg_xZnO_{1-x} Thin films

The resistivity of the Mg_xZnO_{1-x} thin films by (CSP) technique decreases linearly with increasing temperature indicating the semiconductor behaviour. The electrical resistivity(ρ) of the Mg_xZnO_{1-x} thin films (semiconductor material), their electrical conductivity($\sigma_{D.C}$), carrier mobility(μ_H), Hall coefficients (R_H), carrier concentrations, and the type of the charge carrier have been calculated from Hall measurements. Hall measurements indicate that the Mg_xZnO_{1-x} thin films have two types of conductivity, pure ZnO show n-type conductivity ,and the films which have contents (30,50,70, and 90)% show p-type conductivity.

Hall coefficient (R_H) have been calculated from Hall measurements, at substrate temperature (400) ^{o}C, was their value is negative for pure ZnO. (R_H) and carrier concentration are calculated from equation(6) and the value of (R_H) increases with the increasing of Mg-content in the films, and the values of carrier concentration decrease with the increasing of Mg-content in the films. Hall mobility is calculated from the product of the conductivity and Hall coefficient according to equation (7). It can be seen that the Hall mobility increases randomly with the increasing of Mg-content in the films at (400)^{o}C. At high temperatures (450, and 500) ^{o}C can observe the increases and decreases randomly in (n and μ_H) with Mg-content increase. The overall variation in (n and μ_H) can be understood in terms of the position of MgO in the ZnO lattice. The ZnO film generally grows as an n-type semiconductor, due to the presence of native defects in the form of Zinc interstitials, oxygen vacancies, or both. A decrease in (μ_H) at mixing concentrations may be due to the interstitial occupancy of MgO in the ZnO lattice. The presence of MgO at interstitial sites and grain boundaries in the form of oxide, besides decreasing grain size, may act as scattering centers and result in a decrease in the observed mobility at mixing concentration. Figs. (3a, b, c, and d) show the resistivity, conductivity, mobility and carrier concentration as a function of Mg-content for the Mg_xZnO_{1-x} thin films.
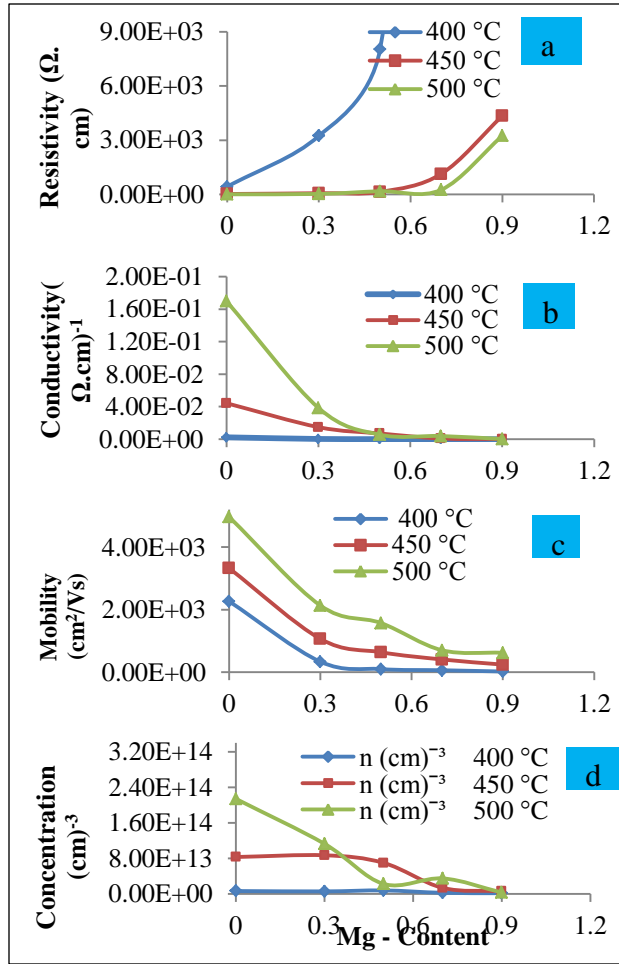
9

Fig.3: The ρ, $\sigma_{D.C}$, μ_H, and n Versus Mg-Content for Mg_xZnO_{1-x} Thin Films at Different Temperatures.

3-5 Raman Shift for Mg_xZnO_{1-x}/n-Si at T_s (400, 450 ,and 500) ^{o}C

Raman scatterings fig.4 confirmed that synthesized Mg_xZnO_{1-x}/n-Si samples have crystalline nature with hexagonal wurtzite structure, but with obvious structural disorder induced by the preparation procedure and presence of impurities. The exact peak positions (frequency) and half-width (FWHM) of each band were determined by Raman spectrometer. To achieve the most accurate deconvolution of the obtained Raman spectra each spectrum was divided into three peaks and analyzed separately. Firstly the low-frequency region $(468)cm^{-1}$ dominated by acoustic overtones, secondly the intermediate frequency region (872) cm^{-1} where optical and acoustic phonon combinations occur, thirdly the high-frequency region (1306) cm^{-1} formed by optical overtones and combinations

for the pure ZnO as shown in fig.4 a. The intense narrow line at (468) cm^{-1} E_2^{high} second-order ZnO Raman mode-associated with the vibration of oxygen atoms, and which dominates the spectra, surely indicates that these are the scatterings from the hexagonal modification of ZnO [18]. Wurtzite type ZnO belongs to the space group C_{6v}^4 and optical phonons belong to the following irreducible representations: $\Gamma_{opt}=A_1+E_1+ 2E_2+2B_1$. The A_1 and E_1 are polar modes and both Raman and infrared active, E_2 are nonpolar and only Raman active, while the B_1 modes are silent [134]. Have tilted orientation the two longitudinal (LO) modes are expected to interact and create one single mode of mixed A_1–E_1 symmetry known as quasi-LO mode where A_1–E_1 symmetry is (872) cm^{-1}, where $E_1(LO)$ frequency is expected to show blue shift while $A_1(LO)$ is almost unaffected by Mg-mixing these results are approaching from the search results[19]. However, due to the two different crystal structures of the Mg_xZnO_{1-x}/n-Si end members the two oxides do not show complete solid solubility, and an intermediate composition range exists in which the composite is phase separated into the wurtzite and cubic structures. For the Raman investigation of the domains with wurtzite and cubic structures, the Raman selection rules need to be considered. According to the Raman selection rules, the scattering of the LO phonon of ZnO with the wurtzite structure is allowed. In contrast, MgO with the cubic rocksalt structure has no allowed first order scattering due to the inversion symmetry of the crystal. However, defects and impurities can destroy the symmetry which in turn may result in first order Raman scattering, a phenomenon that was previously observed in MgO . As can be seen in fig.4 b, the LO mode is found to shift in frequency with Mg-content. Specifically, the LO frequency rises until (30)% Mg-content, which is attributed to the incorporation of Mg into the wurtzite structure. This is expected behavior since the LO mode of MgO is (612) cm^{-1}. Above (30)% Mg, the LO frequency is observed to saturate at (601) cm^{-1} as can be seen in fig. 4c. The saturation is attributed to the wurtzite structure becoming unable to accommodate additional Mg atoms as shown in figs.(4 d, and e). The presence of the cubic phase was confirmed previously XRD.
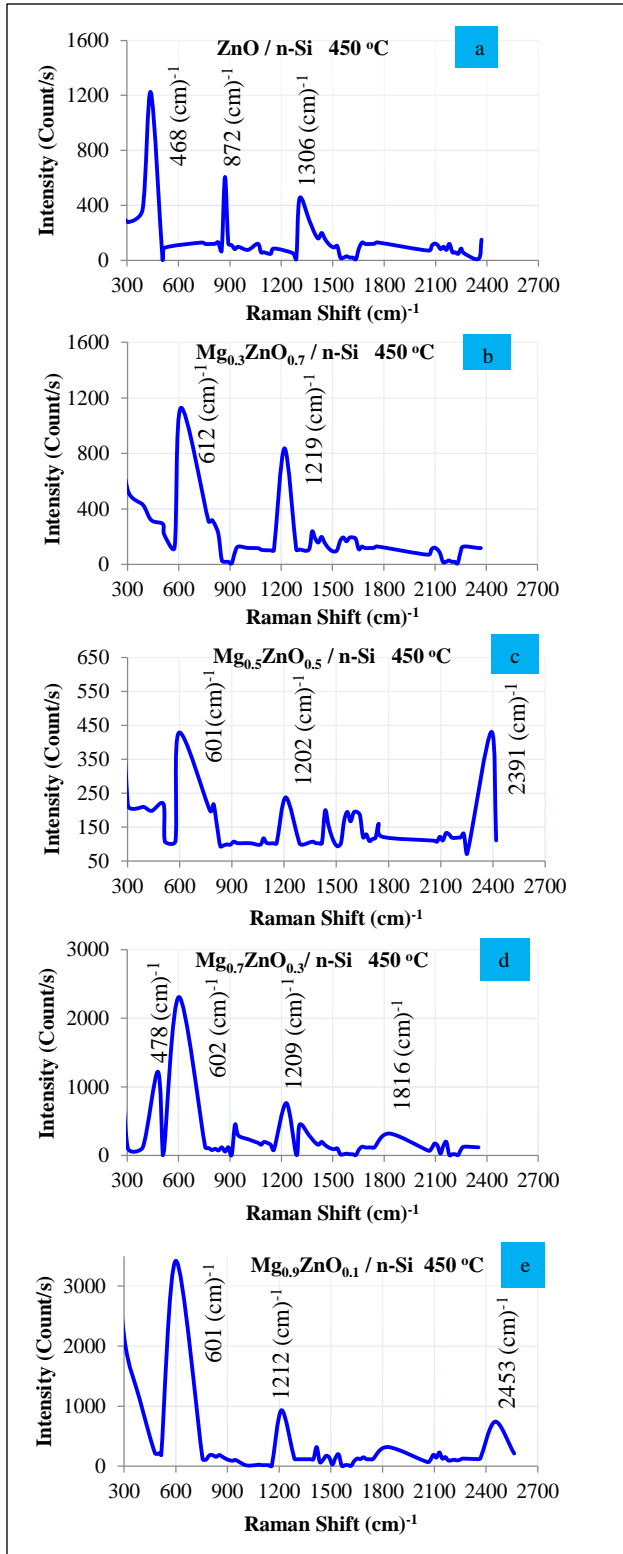
Fig.4: Raman Shift for Mg_xZnO_{1-x}/n-Si Thin Films Prepared in Mg-contents (0, 30, 50, 70, and 90)%, at Substrate Temperature (450) °C.

3-6 Conclusions

Through what has been discussed in the text of paper, it can be concluded the following points:

1. The addition of Mg to the films increases the her strength to withstand high temperatures and little of expansion.
2. All films have polycrystalline structure with an average crystalline size of the molecules smaller than (42.18) nm, also note the decrease in the average of crystalline size with increasing of Mg-content, this shows to the change in the structural properties of the thin films prepared.
3. Through the diagnosis of (XRD) and we found there are three phases of overlaid, the first phase remains structure of the hexagonal wurtzite, but down the intensity of the diffraction peaks, the second phase turns into a mixture of MgO is incorporated with ZnO, the third phase turns into the cubic rock salt structure and the appearance of MgO diffraction peaks are clear.
4. The structural of the ZnO films are found what dependent on the films mixed, (i.e. an increase of the mixture concentration into the film). The results of (XRD) shows that all thin films (pure and mixed) exhibit polycrystalline nature, and has the hexagonal wurtzite structure with preferential orientation in the (002) plane, when the Mg-content ratio (30)%, It turns into a cubic rock salt structure when increasing the Mg-content ratios higher than (50)% with preferential orientation in the (200) plane.

References

[1] C. Kittel, "Introduction to Solid State Physics", 5th edition, John. Wiley and Sons, USA, (1976).

[2] K. Saremah, R. Sarma and H.L. Das , "Correlative assessment of structural and photoelectrical properties of thermally evaporated CdSe thin films", Journal of Non-Oxide Glasses ,Vol.1, pp.(143-156),(2009).

[3] N.M. Saeed , "Structural and optical properties of ZnS thin films prepared by spray pyrolysis technique", Journal of

Al-Nahrain University, Vol.14 , pp.(86-92), (2011).

[4]   J. Sengupta, A. Ahmed, and R. Labar, "Structural and optical properties of post annealed Mg doped ZnO thin films deposited by the sol-gel method", Materials Letters, Vol.109 , pp. (265-268), (2013).

[5]   A. H. Moharram, S. A. Mansour, M.A. Hussein, and M. Rashad,"Direct precipitation and characterization of ZnO nanoparticles" ,Journal of Nanomaterials, Vol. 2014, pp. (1-5), (2014).

[6]   A. Ivashchenko and I. Kerner, "Physical approaches to improvement of semiconductor Gas sensor based on SnO_2 thin films", Moldavian Journal of the Physical Sciences, Vol. 2, pp.(95-102), (2003).

[7]   T. Allen, S. Rutherford, S. Murray, S. Reipert, and M. Goldberg, "Scanning probe and scanning electron microscopy", Elsevier Science (USA), (2006).

[8]   F.H. Abdulrazzak Aldahlaki, "Synthesis and applications of carbon nanotubes", Ph.D. Thesis, University of Babylon-college of science ,chemistry department, Babylon, (2015).

[9]   P.V. Avramov, B.I. Yakobson, and G.E. Scuseria, "Effect of carbon network defects on the electronic structure of semiconductor single-wall carbon nanotubes", Physics of the Solid State, Vol.46, pp.(1168-1172), (2004).

[10] P.-C. Ma, N.A. Siddiqui, G. Marom, and J.-K. Kim, "Dispersion and functionalization of carbon nanotubes for polymer-based nanocomposites a review", Composites: A, Vol.41, pp.(1345-1367), (2010).

[11] S. Byrne, "Raman spectroscopy and X-ray diffraction studies of ZnO grown by pulsed laser deposition", M.Sc. Thesis, School of Physical Sciences, Dublin City University, (2003).

[12] D.C. Look," Methods in materials", John Wiley, New York , p.15 , (2000).

[13] B. R. Nag, "Electron transport in compound semiconductors", Journal Applied Spring-Verlag Berlin Heiderg, New York, (1980).

[14] Y. Yu. Peter,and M. Cardona , "Fundamentals of semiconductors", 3rd edition, Physics and Materials Properties, Springer, p.639, (2005).

[15] S.S. Hullavarad, N.V. Hullavarad, D.E. Pugel, S. Dhar, I. Takeuchi, and R. D. Vispute, "Homo - and hetero-epitaxial growth of hexagonal and cubic $Mg_xZn_{1-x}O$ alloy thin films by pulsed laser deposition technique", Journal of Physics D: Applied Physics, Vol. 40, pp.(4887-4895), (2007).

[16] M. S. Kim, K. T.Noh, K. G. Yim, S. Kim, G. Nam, D.-Y. Lee, J. S. Kim, J. S. Kim, and J.-Y. Leem, "Composition dependence on structural and optical properties of $Mg_xZn_{1-x}O$ thin films prepared by Sol-Gel method", Bull. Korean Chem. Soc.,Vol.32, pp.(3453- 3458), (2011).

[17] T. B. Ivetic, M. R. Dimitrievska, N. L. Fincur, L. R. Đacanin, I. O. Gúth, B.F. Abramovic, and S. R. Lukic- Petrovic, "Effect of annealing temperature on structural and optical properties of Mg-doped ZnO nanoparticles and their photocatalytic efficiency in alprazolam degradation", Ceramics International, Vol. 40, pp.(1545-1552), (2014).

[18] R. Cusco, E. A. Lladó, J. Ibáñez, and L. Artús,"Temperature dependence of Raman scattering in ZnO", Physical Review B75, pp.(1-11), (2007).

[19] N. Kılınc, L. Arda, S. Öztürk, and Z.Z. Öztürk,"Structure and electrical properties of Mg-doped ZnO nanoparticles", Cryst. Res. Tech., Vol.45, pp.(529–538), (2010).